Absence of CO2 electroreduction on copper, gold and silver electrodes without metal cations in solution

Absence of CO_2 electroreduction on copper, gold and silver electrodes without metal cations in solution

Mariana C. O. Monteiro[1], Federico Dattila[2], Bellenod Hagedoorn[1], Rodrigo García-Muelas[2], Núria López[2], Marc T. M. Koper[1,*]

[1]Leiden Institute of Chemistry, Leiden University, P.O. Box 9502, 2300 RA Leiden, The Netherlands

[2]Institute of Chemical Research of Catalonia (ICIQ), The Barcelona Institute of Science and Technology (BIST), Av. Països Catalans 16, 43007 Tarragona, Spain.

Supplementary Information

Supplementary Discussion

Hanging meniscus experiments

Characterization of the polycrystalline gold electrode

Before all the CO_2 reduction experiments in hanging meniscus configuration were performed, the gold electrode was flame annealed using the protocol previously described[1] and the electrode was characterized in 0.1 M H_2SO_4. The characterization by cyclic voltammetry (CV) was done in between all measurements, to assure a reproducible surface which allows for comparison of the CO_2 reduction results and determination of the electrochemical active surface area. The characterization CVs recorded during the hanging meniscus experiments presented in the main text can be found in Supplementary Figure 1.

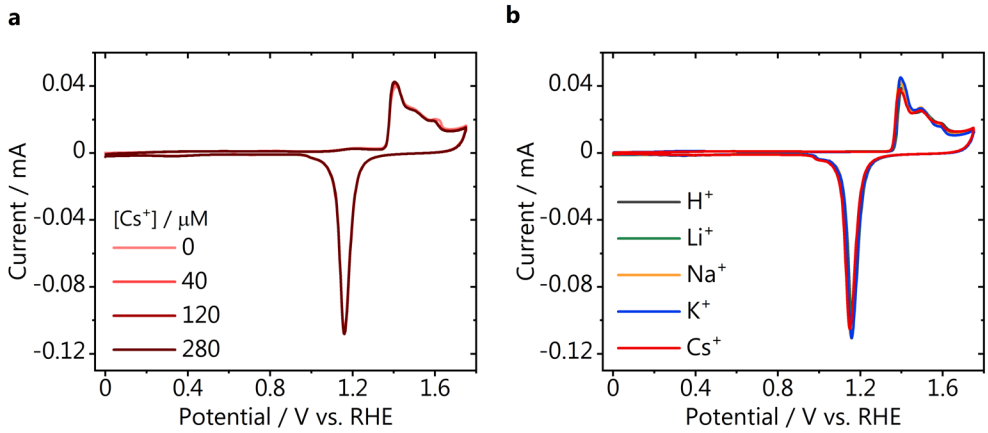

Supplementary Figure 1. Blank voltammetry of the gold electrode used in the hanging meniscus experiments after surface preparation through polishing and flame annealing. **a**, CVs recorded before the measurements in 1 mM H_2SO_4 with the addition of different amounts of Cs^+, **b**, CVs recorded before the measurements in 1 mM M_2SO_4 (*M* = H, Li, Na, K, Cs).

Hydrogen evolution and CO_2 reduction in 1mM M_2SO_4 (*M* = H, Li, Na, K, Cs)

Hydrogen evolution and CO_2 reduction were also carried out in 1 mM sulfate solutions of different cations, all adjusted to pH = 3 when necessary. The cyclic voltammetry can be seen in the figure below, together with the results obtained in 1 mM H_2SO_4, for comparison. To calculate the CO oxidation charge density shown in the main text, the double layer charge recorded in Argon was subtracted from the total charge found in CO_2 atmosphere.

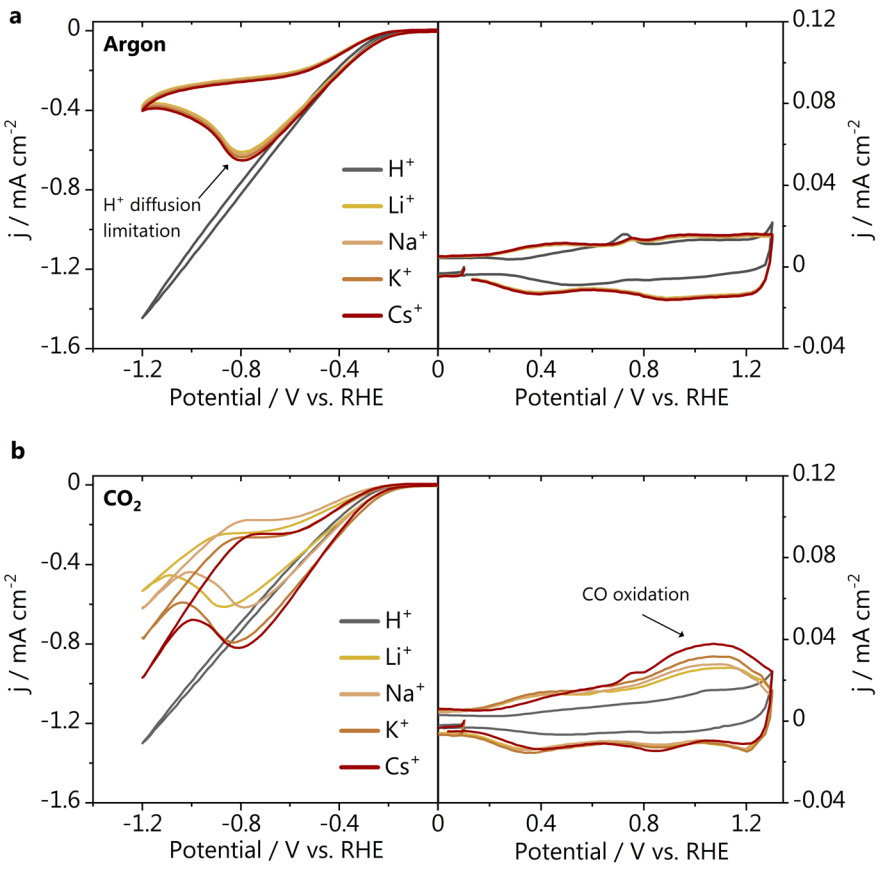

Supplementary Figure 2. Cyclic voltammetry recorded in **a**, argon and **b**, CO_2 atmosphere on gold in 1 mM M_2SO_4 (*M* = H, Li, Na, K, Cs) at pH = 3 (50 mV s^{-1}).

CO oxidation control experiment

A control experiment was performed to show that CO can be oxidized on the gold electrode in the absence of a metal cation in the electrolyte. Before the measurement the gold electrode was characterized in argon saturated 0.1 M H_2SO_4 electrolyte. The 0.1 M H_2SO_4 electrolyte was saturated with CO for 5 minutes and subsequently a cyclic voltammogram was recorded. Supplementary Figure 3 displays both CVs, in which the large anodic current (red curve) starting at 0.8 V vs RHE shows that CO can be oxidized without a metal ion in solution.

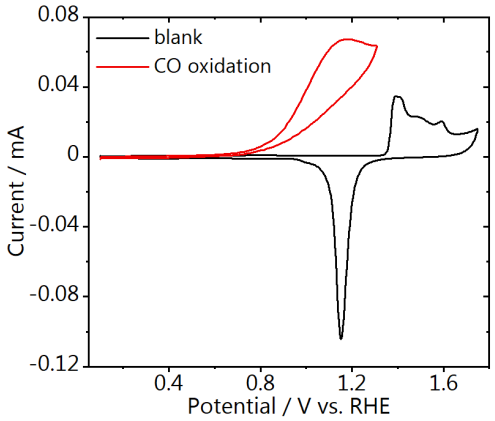

Supplementary Figure 3. CO oxidation voltammetry on gold recorded in 0.1 M H_2SO_4 after saturation the electrolyte with CO (50 mV s^{-1}).

CO_2 reduction in 1mM H_2SO_4 + µM Cs^+

CVs were recorded directly after the CO_2 reduction cathodic scan from 0 to –1.2 V vs. RHE in 1 mM H_2SO_4 in order to semi-quantitatively determine the amount of CO produced with and without the addition of different amounts of Cs^+. The three subsequently cycles recorded are shown in Supplementary Figure 4a-c and the first cycles are shown in the main text. The increase in the amount of CO produced over the 3 cycles for each concentration is likely due to an accumulation of CO_2 near the surface after CO oxidation. Additionally, considering a direct competition between proton and CO_2 reduction, an increase of the interfacial pH and consequent suppression of proton reduction, could lead to more CO produced.

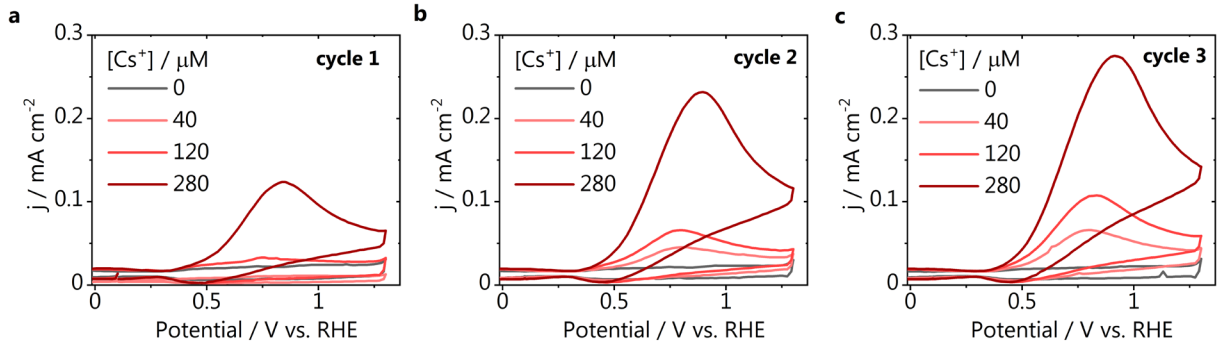

Supplementary Figure 4. a, First, **b**, second and **c**, third cycles recorded at 50 mV s^{-1} on a gold electrode directly after a cathodic scan in CO_2 atmosphere when different amounts of Cs^+ were added to the 1 mM H_2SO_4 electrolyte.

CO_2 reduction in Li_2SO_4 + µM Cs^+

Li_2SO_4 was used as background electrolyte to investigate the effect of the Cs^+ concentration in the CO production. The cathodic and subsequently anodic cyclic voltammetry recorded can be seen in Supplementary Figure 5.

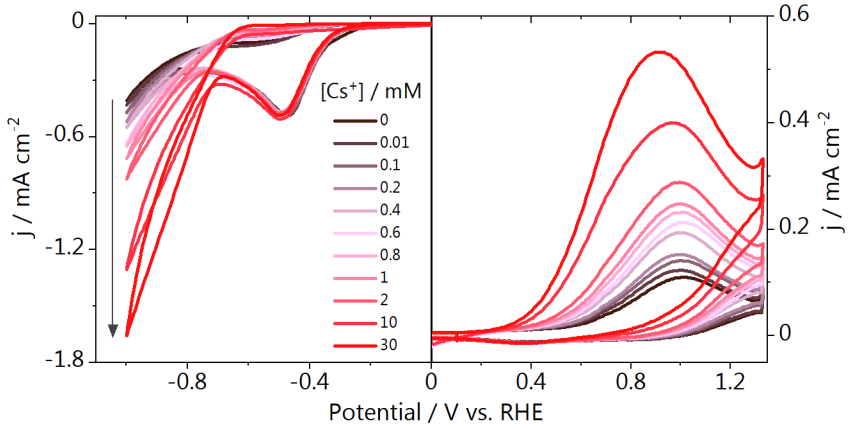

Supplementary Figure 5. Cyclic voltammetry recorded at 50 mV s^{-1} during CO_2 reduction on gold in Li_2SO_4 electrolyte contaning different concentrations of Cs^+. The total cation concentration in solution was kept 0.1 M and the pH = 3.

SECM experiments

Capacitive approach curve fitting

A capacitive approach in air is performed before the SECM measurements in order to determine the tip-to-surface distance. The approach curve is constructed by applying an AC voltage to the sample and recording the capacitive current generated at the tip as a function of position until reaching the exponential regime of the capacitance. The position is converted to distance by fitting the approach curve with Supplementary Equation 1, which provides the absolute surface position (d_0). This fitting function is different than the one presented in our previous work[2]. It describes the system as a point charge in front of a plate, instead of a pure parallel plate capacitor, which we find to give a more precise estimation of d_0.[3]

$$C_{tot}(Z) = -A_1 * \ln(d_0 - Z) + \mathrm{B} + \left(\frac{A_2}{L_{par} + d_0 - Z}\right) \quad (1)$$

Supplementary Figure 6 shows the Pt-UME approach curves recorded before the SECM experiments performed using the gold, silver and copper samples. The fit is shown in red.

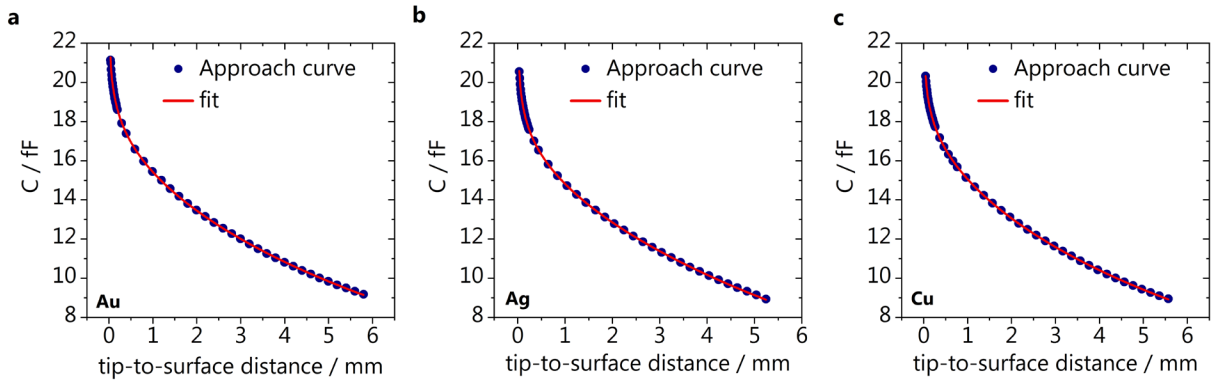

Supplementary Figure 6. Capacitive approach curves recorded before the SECM experiments on **a**, gold, **b**, silver and **c**, copper.

Stability of the silver and copper electrodes

Supplementary Figure 7 shows the instability of the silver and copper electrodes when potentials more cathodic than –0.8 and –1 V vs. RHE are applied to the sample, respectively. It shows different cycles of the Pt-UME voltammetry recorded subsequently, either after hydrogen evolution or CO_2 reduction are carried out at the sample. As can be seen in Supplementary Figure 7a when CO_2 reduction is performed on silver in 1 mM H_2SO_4 at –1 V vs. RHE, CO is produced, at small amounts. This goes against what was observed in all the other experiments shown in the main text, in which CO_2 reduction does not take place at all without a metal ion in solution. The difference here, is that under this cathodic potential Ag^+ ions go into solution, enabling the CO_2 reduction reaction.[4] This happens as due to the SECM capacitive approach, the sample is exposed to air for a relatively long period of time, which likely leads to the formation of a very small amount of oxide. The presence of Ag^+ ions in the electrolyte can be confirmed looking at the 5th cycle recorded from the Pt-UME shown in Supplementary Figure 7b, which presents voltammetric features characteristic of the underpotential deposition of Ag^+ on polycrystalline platinum.[5] The same happens with the copper sample when polarized more negatively than –1 V vs. RHE. Copper deposition is observed in the Pt-UME voltammetry and can be seen in Supplementary Figure 7c.[6] These observations were made when either HER or CO_2 reduction were performed at the sample and are crucial for the correct execution and judgment of the experimental results. In between measurements, the SECM cell was always fully disassembled and thoroughly cleaned as here we observed that trace amounts of metal ions can already lead to the production of CO.

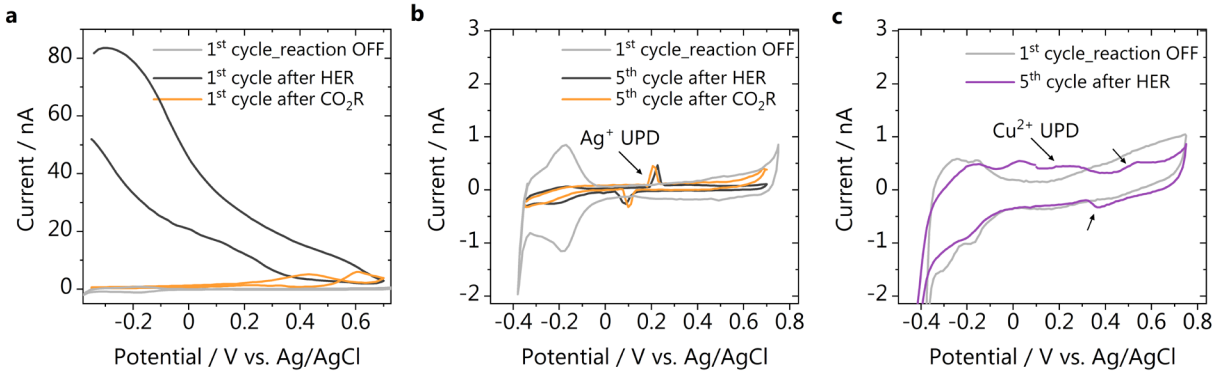

Supplementary Figure 7. Pt-UME voltammetry **a**, after HER or CO_2 reduction are performed on silver in 1 mM H_2SO_4 and **b**, subsequent cycles from the same experiment showing the presence of Ag^+ ions in the electrolyte and **c,** similar observations on the copper electrode.

Supplementary Methods

Model

An accurate density functional theory (DFT) modeling of the interaction between ions and water molecules close to the catalytic surface requires *ab initio* molecular dynamics (AIMD) simulations with a suitable number of explicit solvent molecules and a proper choice of the equilibration time. Generally, at least 4 water bilayers are required, as well as at least 10 ps of equilibration time.[7] Since platinum and gold present similar structural properties, we inherited an explicit solvation configuration equilibrated for 11 ps of AIMD on (3√3×3√3)*R*30° Pt(111) at 300 K (4 water bilayers, 72 water molecules).[7] The pre-equilibrated water molecules were inserted on top of a (3√3×3√3) *R*30° Au(111) (4 layers, 15.3 Å × 15.3 Å × 30.0 Å, 8 Å vacuum thickness) and let further equilibrate for 2 ps with time steps of 1 fs at 300 K on the gold supercell (Supplementary Figure 8a). This system was named Au-H_2O, since it reproduces the cation-free experimental sample. After this equilibration, an alkali atom (Li, Na, K, or Cs) was inserted in a solvation cavity close to the surface (initial $d_{M\text{-surface}}$ = 3.3 Å, Supplementary Figure 9) and the four systems were equilibrated for 2 ps at 300 K (Supplementary Figure 8b). A hydrogen was removed from a water molecule in the fourth water bilayer, so that the +1 $|e^-|$ charge of the cation was balanced by the –1 $|e^-|$ charge of the resulting OH^-. These systems were classified as Au-H_2O-M^+ where M^+ stands for Li^+, Na^+, K^+, and Cs^+. Given the thickness of the solvation layer, around 1.4 nm, Au geometrical area, 2.0 nm^2, and the number of water molecules, 72, the cation surface concentration is between 0.5 ($1/N_A$ mol of cation within V = 3.29 nm^3) and 0.8 M (1/72 of water molar concentration, 55.5 M). Finally, a CO_2 molecule was inserted close to the surface for both Au-H_2O and Au-H_2O-M^+ systems, with a surface coverage of 0.04 ML (1 molecule for 27 Au surface atoms), as shown in Supplementary Figure 8c. Upon interaction with solvation molecules and cation during 2 additional ps at 300 K, CO_2 adsorbed on the surface *via* a $\eta^2_{C,O}$ conformation (bidentate through carbon and one oxygen) and the second oxygen coordinated to the alkali cation or to water molecules through H-bonds. These final systems were labelled Au-H_2O-CO_2 and Au-H_2O-M^+-CO_2.

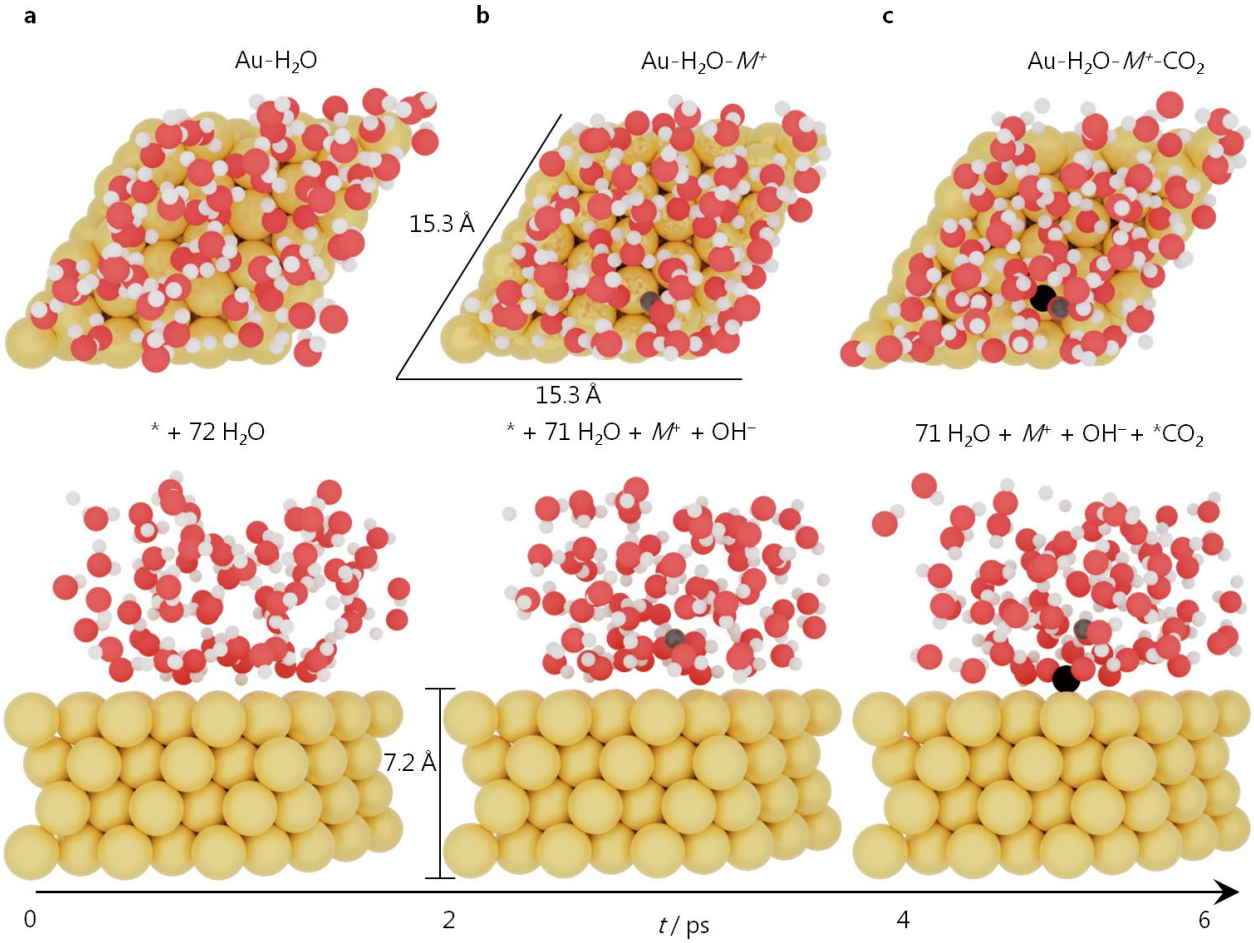

Supplementary Figure 8. Input models for *ab initio* molecular dynamics simulation carried out on a (3√3x3√3)*R*30° Au(111) supercell (15.3 Å x 15.3 Å x 30.0 Å) with 72 water molecules. **a**, The Au-H_2O system equilibrated for 2 ps (1 fs time step) at 300 K. **b**, Insertion of an alkali cation (Li^+, Na^+, K^+, Cs^+) close to the surface and equilibration for another 2 ps at 300 K. **c**, Addition of a CO_2 molecule to the system, that interacts with the gold surface *via* a $\eta^2_{C,O}$ conformation with one oxygen coordinated to the alkali cation, and AIMD further carried out for 2 ps at 300 K. The portrayed cation is Li^+.

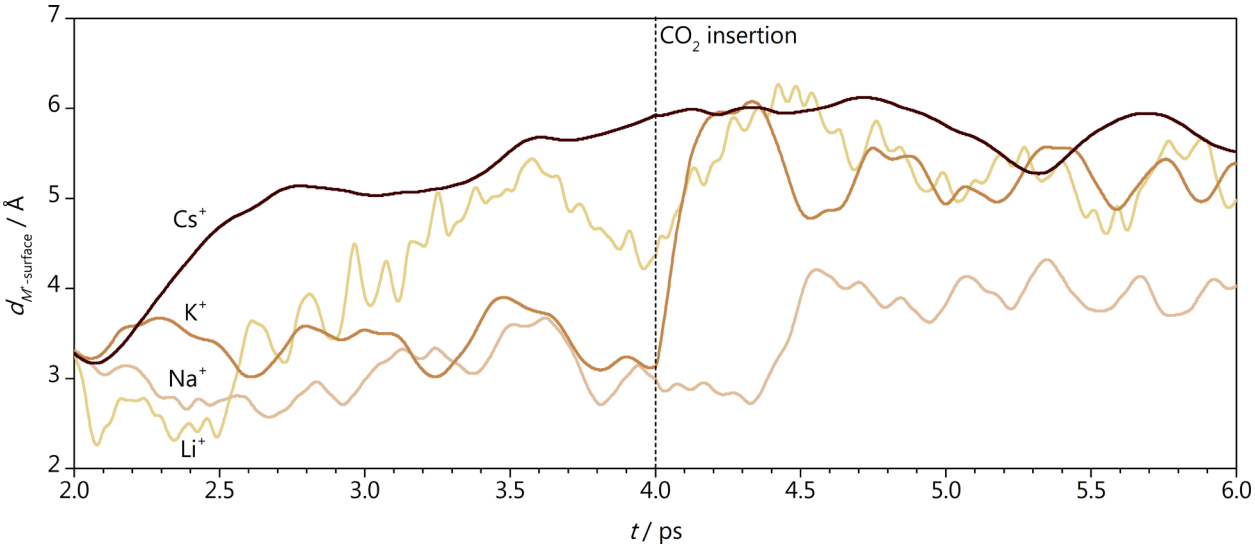

Supplementary Figure 9. Distance between cation (M^+) and surface calculated during equilibration of the Au-H_2O-M^+ system (from 2 to 4 ps) and upon insertion of CO_2 in the vicinity of the cation (from 4 to 6 ps).

Cation-water radial distribution functions

Cation-water radial distribution functions, $g_{M+\text{-}H2O}(r)$ were obtained for the 2 ps equilibration of the Au-H_2O-M^+ systems to account for the density of water molecules around the alkali metal center, M^+. We first calculated the distribution of distances, $\eta(r)$, defined as the number of H_2O oxygens at a distance between r and $r + \Delta r$ for all the molecular dynamics steps, where r is the position vector from the central cation and Δr is its differential. We then normalized $\eta(r)$ for the expected surface density of cations ρ corresponding to 2D annulus formed by the solvation layer, Supplementary Equation 2:

$$g(r)_{2D} = \frac{\eta(r)}{2\pi r \cdot \Delta r \cdot \rho} \quad (2)$$

where $g(r)$ is the radial distribution function (dimensionless), $\eta(r)$ the distribution of distances (dimensionless), r the position vector, Δr its differential (both in Å), and ρ the cation surface density ($Å^{-2}$). Cation-water radial distribution functions are reported in Supplementary Figure 10 and the parameters of the Lorentzian fit on the first solvation shell peaks are shown in Supplementary Table 1. A Lorentzian fit was applied through Supplementary Equation 3 and it was preferred to a Gaussian fit since it was numerically more stable:

$$g(r) = g(r)_0 + \left(\frac{2A}{\pi}\right) \cdot \left(\frac{w}{4(r - d_{M^+-O})^2 + w^2}\right) \quad (3)$$

where $g(r)$ is the radial distribution function, r the position vector (Å), w the full width at half maximum (Å), $d_{M+\text{-}O}$ the cation-oxygen bond length (Å), whilst $g(r)_0$ (dimensionless) and A (Å) are fit parameters. For larger alkali cations, the first solvation shell becomes softer as indicated by the broadening of the first $g_{M+\text{-}H2O}(r)$ peak and the increase of w (Supplementary Table 1). For Cs^+ the transition between first, second, and third solvation shell is continuous, therefore this alkali metal can easily modify its coordination. The parameters of the Lorentzian fit (dashed lines) and the consequent estimation of the cation-oxygen distances in the first solvation shell are reported in Supplementary Table 1 and agree with

previous experimental and theoretical reports.[8,9] The cation-oxygen bond length ($d_{M^+\text{-O}}$) and its associated uncertainty are obtained from the fit parameters on the $g(r)$ first peaks. The term $d_{M^+\text{-O(S.A.)}}$ stands for averages of state-of-the-art values for cation-water distances.[8,9]

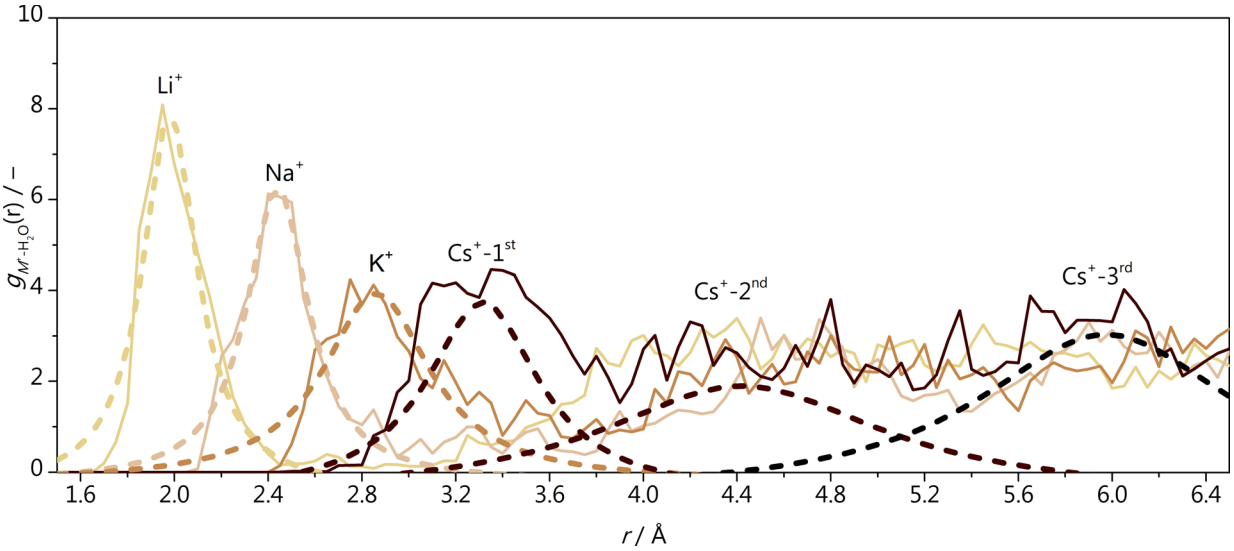

Supplementary Figure 10. Cation solvation shells during 2 ps equilibration of the Au-H_2O-M^+, described by the cation-water radial distribution functions.

Supplementary Table 1. Parameters of the Lorentzian fit and distances between cation and water molecules in the first solvation shell, estimated from the position of the first peak of cation-water radial distribution functions, Supplementary Figure 10. $g(r)_0$, A, w(Å), χ^2_ν and $d_{M^+\text{-O}}$ (Å) are fit parameters with the associated fit uncertainties. The state-of-the-art values for cation-water distances, $d_{M^+\text{-O(S.A.)}}$ (Å), and associated uncertainties are taken from Ref.[9] .

M^+	$g(r)_0$ / –	A / Å	w / Å	χ^2_ν / –	$d_{M^+\text{-O}}$ / Å	$d_{M^+\text{-O(S.A.)}}$ / Å
Li$^+$	–0.39 ± 0.16	3.7 ± 0.3	0.28 ± 0.02	0.34	1.981 ± 0.007	2.08 ± 0.07
Na$^+$	–0.22 ± 0.08	3.3 ± 0.2	0.32 ± 0.02	0.12	2.440 ± 0.005	2.36 ± 0.06
K$^+$	–0.22 ± 0.12	3.6 ± 0.4	0.55 ± 0.06	0.22	2.86 ± 0.02	2.80 ± 0.08
Cs$^+$-1st	–0.53 ± 0.12	3.9 ± 0.6	0.58 ± 0.07	0.21	3.32 ± 0.02	3.14 ± 0.08
Cs$^+$-2nd	–0.53 ± 0.12	6 ± 2	1.5 ± 0.4	0.21	4.42 ± 0.08	–
Cs$^+$-3rd	–0.53 ± 0.12	7 ± 2	1.3 ± 0.4	0.21	5.97 ± 0.06	–

Cation coordination number

To obtain the coordination number $N_{M^+\text{-O}}$ of the alkali cations M^+, we assigned a bond value equal to one if the cation-oxygen distance $r_{M^+\text{-O}}$ was equal or lower than the cation-oxygen bond length $d_{M^+\text{-O}}$, Supplementary Table 1. Otherwise, the bond value was set to zero if $r_{M^+\text{-O}}$ was larger than a certain threshold $th_{M^+\text{-O}}$: 2.5, 3.0, 3.5, 4.0 Å for Li$^+$, Na$^+$, K$^+$, and Cs$^+$, respectively (Supplementary Figure 10). Between these extremes, $N_{M^+\text{-O}}$ was calculated through Supplementary Equation 4 following a decay controlled by the error function (erf), Supplementary Equation 5.[10] In Supplementary Equation 4, $N_{M^+\text{-O}}$ is the cation coordination number (dimensionless), $r_{M^+\text{-O}}$ is the cation-oxygen distance (Å), $d_{M^+\text{-O}}$ the cation-

oxygen bond length (Å), $th_{M+\text{-O}}$ the cation-oxygen threshold (Å) and avg stands for average. In Supplementary Equation 5, *t (*dimensionless*)* is the variable of integration and 0 and *z* represent the integration limits.

$$N_{M^+-\mathrm{O}} = \frac{1}{2} - \frac{1}{2}\,\mathrm{erf}\left(\frac{r_{M^+-\mathrm{O}} - \mathrm{avg}(d_{M^+-\mathrm{O}}, th_{M^+-\mathrm{O}})}{0.2\ \text{Å}}\right) \quad (4)$$

$$\mathrm{erf}(z) = \frac{2}{\sqrt{\pi}} \int_0^z \exp(-t^2)\, dt \quad (5)$$

Supplementary Table 2. Cation coordination numbers to oxygen atoms in water ($N_{M+\text{-O(H2O)}}$) and CO_2 ($N_{M+\text{-O(CO2)}}$) in presence and absence of adsorbed CO_2 as calculated through Supplementary Equation 4. Cation coordination to water molecules or CO_2 was calculated for Au-H_2O-M^+ and Au-H_2O-M^+-CO_2 during 2 ps AIMD at 300 K. Coordination numbers are reported as averages with their associated standard deviation $\sigma(N_{M^+\text{-O}})$, median, maximum, and minimum values.

	$N_{M+\text{-O(H2O)}}$ (Au-H_2O-M^+)				$N_{M+\text{-O(H2O)}}$ (Au-H_2O-M^+-CO_2)				$N_{M+\text{-O(CO2)}}$ (Au-H_2O-M^+-CO_2)			
M^+	Mean	Median	Max	Min	Mean	Median	Max	Min	Mean	Median	Max	Min
Li^+	2.8 ± 0.8	2.9	3.9	0.3	3.2 ± 0.5	3.3	3.9	1.8	0.1 ± 0.3	0.0	1.0	0.0
Na^+	3.2 ± 0.5	3.0	4.7	2.1	2.3 ± 0.4	2.3	3.0	1.2	0.9 ± 0.2	1.0	1.0	0.0
K^+	3.5 ± 0.9	3.4	4.9	1.1	3.6 ± 0.6	3.7	4.9	1.7	0.9 ± 0.4	1.0	2.0	0.0
Cs^+	5.8 ± 1.2	5.9	8.0	2.9	5.4 ± 0.9	5.4	6.9	3.6	1.3 ± 0.5	1.1	2.0	0.0

Supplementary Table 3. Average CO_2 adsorption Gibbs free energy ΔG_{*CO2} (eV) and cation induced stabilization, $\Delta\Delta G_{*CO2}$ (eV). ΔG_{*CO2} are reported with their associated standard deviations $\sigma(\Delta G_{*CO2})$. The systems under study were Au-H_2O-CO_2 and Au-H_2O-CO_2-M^+ equilibrated for 1 and 2 ps AIMD respectively. The explicit solvent layer includes 72 H_2O molecules. Those containing cations have a water molecule replaced by M^+OH.

System	ΔG_{*CO2} / eV	$\Delta\Delta G_{*CO2}$ / eV
H_2O	+0.80 ± 0.18	–
Li^+	+0.16 ± 0.24	–0.64
Na^+	+0.28 ± 0.18	–0.53
K^+	+0.41 ± 0.12	–0.39
Cs^+	+0.23 ± 0.21	–0.58

Supplementary Table 4. Average CO_2 adsorption Gibbs free energy ΔG_{*CO2} (eV), CO_2 activation angle α (degrees), Bader charges for CO_2 intermediate and cation M^+, either coordinated to CO_2 or in the reference system (CO_2 removed), reported in elementary charge ($|e^-|$) and net CO_2 surface normal electric dipole moment $\vec{p}$ reported in $|e^-|$Å. Uncertainties are given as the standard deviation of the data. For cation Bader charges, $\Delta q \leq 0.01\ |e^-|$.

System	ΔG_{*CO2} / eV	α / °	q_{CO2} / $\lvert e^-\rvert$	$q_{M+(CO2)}$ / $\lvert e^-\rvert$	$q_{M+(ref)}$ / $\lvert e^-\rvert$	$\vec{p}_{CO2}$ / $\lvert e^-\rvert$Å
H_2O	+0.80 ± 0.18	137 ± 5	–0.47 ± 0.10	–	–	+0.40 ± 0.09
Li^+	+0.16 ± 0.24	133 ± 5	–0.67 ± 0.08	–0.91	–0.90	+0.66 ± 0.11
Na^+	+0.28 ± 0.18	134 ± 5	–0.65 ± 0.08	–0.91	–0.90	+0.54 ± 0.08
K^+	+0.41 ± 0.12	136 ± 3	–0.58 ± 0.09	–0.91	–0.90	+0.54 ± 0.09
Cs^+	+0.23 ± 0.21	131 ± 4	–0.71 ± 0.08	–0.91	–0.91	+0.65 ± 0.13

Supplementary Note 1

Cation-induced electric field

We estimated the cation-induced electric field following a similar procedure as introduced by Chen *et al.*[11] First, we calculated the electrostatic potential induced by the cation upon removal of the CO_2 intermediate through Supplementary Equation 6, where $U_{\text{surf+solv+ion}}$, $U_{\text{surf+solv}}$, U_{ion} indicate the electrostatic potential for the overall system (surface, solvation and ion), the environment (surface and solvation), and the ion alone respectively. Then, assuming the cation as a point charge, we define the local electric field $\vec{E}_{\text{el}}$ through Supplementary Equation 7, where $U(\vec{r})$ is the cation-induced electrostatic potential difference at a given coordinate $\vec{r}$. $\vec{r}_{\text{ads}}$ and $\vec{r}_{M+}$ represent the adsorbate and cation positions, respectively. The additional negative sign is introduced to assess the electric field induced on a negatively charged adsorbate, such as $*CO_2^-$.

$$U(\vec{r}) = U_{\text{surf+solv+ion}} - U_{\text{surf+solv}} - U_{\text{ion}} \quad (6)$$

$$-\vec{E}_{\text{el}} = -\left(-\frac{U(\vec{r}_{\text{ads}}) - U(\vec{r}_{M+})}{\|\vec{r}_{\text{ads}} - \vec{r}_{M+}\|}\right)\hat{r} \quad (7)$$

We calculated the local electric field around the $*CO_2^-$ adsorbate for different cation configurations over the last 1 ps of AIMD simulation. We applied Supplementary Equation 6 to estimate $\vec{E}_{\text{el}}$ at the position of C, O_1, and O_2 and then we plotted the averaged value versus the average between cation-(C, O_1, O_2) distances and cation-water coordination numbers. The electric field distribution is affected by both d(M^+,{C,O_1,O_2}) and the instantaneous coordination number $N(M^+–O(H_2O))$ and highest intensities are reported for low cation-water coordination numbers and short distances, in agreement with a recent theoretical characterization for electrochemical CO_2 reduction on gold.[12]

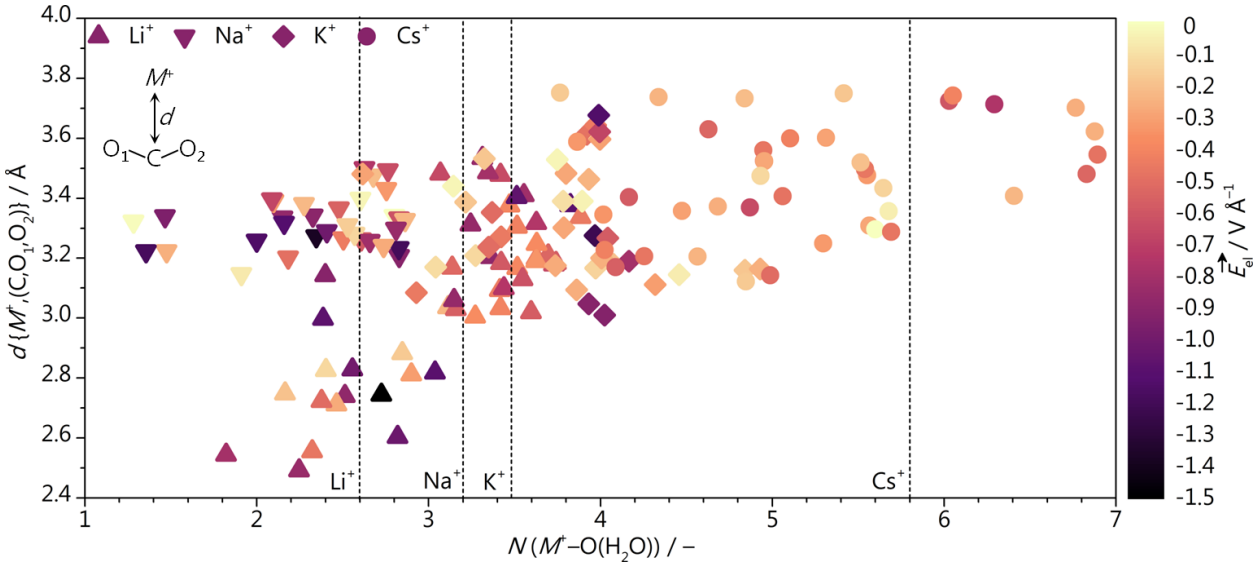

Supplementary Figure 11. Cation-induced electric field as a function of the cation-water coordination number, $N(M^+–O(H_2O))$, (horizontal axis) and the average between cation-(C,O_1,O_2) distances (vertical axis) for different AIMD configurations. ▲, ▼, ♦, and ● represent Li^+, Na^+, K^+, and Cs^+ respectively. Dashed lines represent average cation-water coordination numbers and are taken from Supplementary Table 2.

Supplementary Note 2

Electric dipole effects

Intermediates with large electric dipole moments are affected by electrostatic fields across the electrical double layer (EDL), and their Gibbs free energy of adsorption changes according to Supplementary Equation 8.[13] Thus, the stabilization (or destabilization) of adsorbates depends on their net electric dipole moment $\vec{p}$ and their relative orientation with respect to the electric field $\vec{E}_{\mathrm{el}}$ within the EDL. The electric field is caused by the electric potential U applied to the electrode with respect to its potential of zero charge U_{pzc} (+0.2 V vs. SHE for polycrystalline gold[14]), and the contribution of neighboring ions, $\vec{E}_{\mathrm{el-ion}}$, which is in the order of 1 V Å^{-1}.[11,15] In Supplementary Equation 8 *d* stands for the thickness of the EDL, which is usually assumed around 3 Å.[11,13,16]

$$\Delta G = +\vec{p}\cdot\vec{E}_{\mathrm{el}} = +\vec{p}\cdot\left(\frac{U-U_{\mathrm{pzc}}}{d}\hat{z}+\vec{E}_{\mathrm{el-ion}}\right) \quad (8)$$

Given the electric dipole moments calculated for adsorbed CO_2 (Supplementary Table 4), we estimated that the stabilization for CO_2^- adsorption due to dipole/electric field interactions adds up to 0.6 eV in the presence of a partially desolvated neighboring cation ($\vec{E}_{\mathrm{el}}$ = 1 V Å^{-1}, Supplementary Figure 12). These values agree with the change in the Gibbs free energy of adsorption for CO_2^- due to cation-CO_2 interaction (Figure 7 in the Main Text). In the absence of a cation, a cathodic potential as negative as –3.0 V vs. RHE is required to induce an equivalent electric field. Therefore, under standard CO_2 reduction conditions the cation is key to open the reduction reaction pathway *via* explicit ionic bond with negatively charged intermediate and explicit, short-range dipole/cation-induced electric field effect.

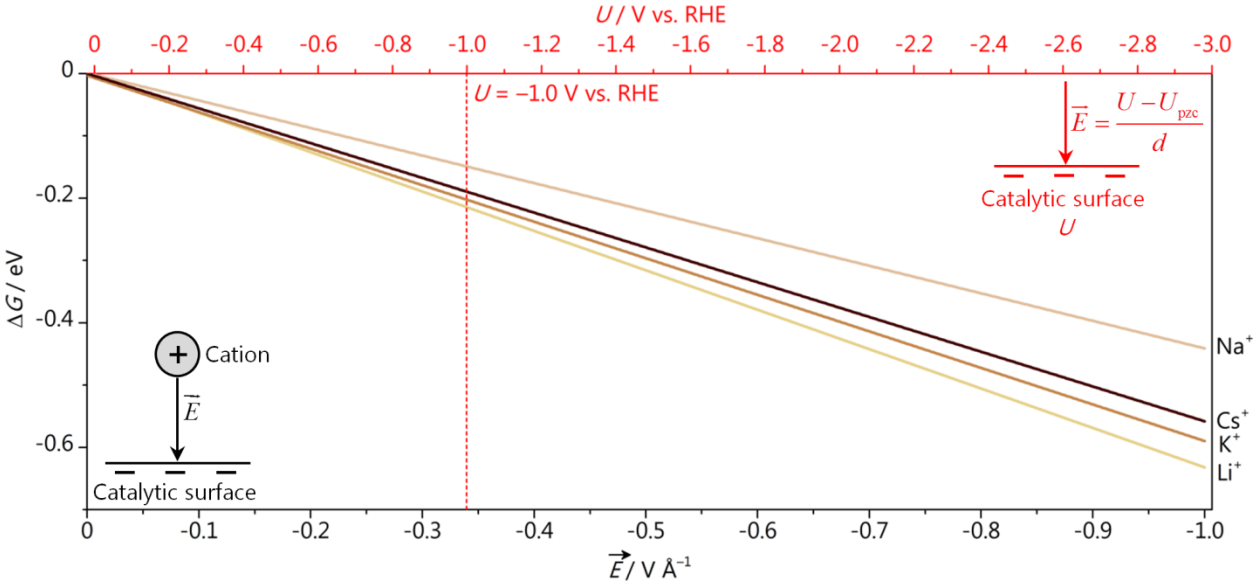

Supplementary Figure 12. Stabilization of CO_2 adsorption due to the interaction between CO_2 dipole moment and local electric field generated by the cation (bottom axis, inset on the left). Top *x*-axis (red, inset on the right) reports the cathodic potential needed to achieve an equivalent electric field in absence of cation, according to Supplementary Equation 8 and assuming an EDL thickness, *d*, of 3 Å.[11,13,16] Red dashed line indicates the potential applied during the study of CO production vs. Cs^+ concentration on gold (Figure 2).

Supplementary References

1. Monteiro, M. C. O. & Koper, M. T. M. Alumina contamination through polishing and its effect on hydrogen evolution on gold electrodes. *Electrochim. Acta* **325**, 134915 (2019).

2. Monteiro, M. C. O., Jacobse, L., Touzalin, T. & Koper, M. T. M. Mediator-Free SECM for Probing the Diffusion Layer pH with Functionalized Gold Ultramicroelectrodes. *Anal. Chem.* **92**, 2237–2243 (2020).

3. Monteiro, M. C. O., Jacobse, L. & Koper, M. T. M. Understanding the Voltammetry of Bulk CO Electrooxidation in Neutral Media through Combined SECM Measurements. *J. Phys. Chem. Lett.* **11**, 9708–9713 (2020).

4. Henckel, D. A. *et al.* Potential Dependence of the Local pH in a CO_2 Reduction Electrolyzer. *ACS Catal.* **11**, 255–263 (2021).

5. Macao, L. H., Santos, M. C., Machado, S. A. S. & Avaca, L. A. Underpotential deposition of silver on polycrystalline platinum studied by cyclic voltammetry and rotating ring-disc techniques. *J. Chem. Soc. - Faraday Trans.* **93**, 3999–4003 (1997).

6. Lukaszewski, M., Soszko, M. & Czerwiński, A. Electrochemical methods of real surface area determination of noble metal electrodes - an overview. *Int. J. Electrochem. Sci.* **11**, 4442–4469 (2016).

7. Bellarosa, L., García-Muelas, R., Revilla-López, G. & López, N. Diversity at the Water–Metal Interface: Metal, Water Thickness, and Confinement Effects. *ACS Cent. Sci.* **2**, 109–116 (2016).

8. Waegele, M. M., Gunathunge, C. M., Li, J. & Li, X. How cations affect the electric double layer and the rates and selectivity of electrocatalytic processes. *J. Chem. Phys.* **151**, 160902 (2019).

9. Marcus, Y. Ionic radii in aqueous solutions. *Chem. Rev.* **88**, 1475–1498 (1988).

10. Dattila, F., García-Muelas, R. & López, N. Active and selective ensembles in oxide-derived copper catalysts for CO_2 reduction. *ACS Energy Lett.* **5**, 3176–3184 (2020).

11. Chen, L. D., Urushihara, M., Chan, K. & Nørskov, J. K. Electric Field Effects in Electrochemical CO_2 Reduction. *ACS Catal.* **6**, 7133–7139 (2016).

12. Zhu, Q., Wallentine, S., Deng, G. & Baker, L. R. Solvation-Induced Onsager Reaction Field Rather than Double Layer Field Controls CO_2 Reduction on Gold. 1–11 (2021) Preprint available at doi:10.26434/chemrxiv.14410655.v1.

13. McCrum, I. T., Bondue, C. J. & Koper, M. T. M. Hydrogen-Induced Step-Edge Roughening of Platinum Electrode Surfaces. *J. Phys. Chem. Lett.* **10**, 6842–6849 (2019).

14. White, R. E., Bockris, J. O. & Conway, B. E. *Modern Aspects of Electrochemistry*. (Kluwer Academic Publishers, 2002).

15. Resasco, J. *et al.* Promoter Effects of Alkali Metal Cations on the Electrochemical Reduction of Carbon Dioxide. *J. Am. Chem. Soc.* **139**, 11277–11287 (2017).

16. Nørskov, J. K. *et al.* Origin of the Overpotential for Oxygen Reduction at a Fuel-Cell Cathode. *J. Phys. Chem. B* **108**, 17886–17892 (2004).